communications chemistry

A Nature Portfolio journal

Article

https://doi.org/10.1038/s42004-025-01561-8

Hydrazone-based photocages for precise sub-organelle visualization and drug release

Check for updates

Xia Wang[1,6], Jingming Zhou[1,6], Yu Cheng[2,6], Hongmei Wu[1,3], Xuejing Su[1,4], Rundong Wang[1], Kaiyan Xiao[1], Weiwei Zhang[1,4], Zhong Chen[1], Bing Xu[1], Yusheng Lu[5,7] ✉, Hongqiang Qiu[2,7] ✉ & Lijun Xie[1,7] ✉

Photocages are widely investigated for their bioimaging, controlled drug release, and cellular process modulation. Developing universal photoactive units can significantly expand the structural diversity of photocages. Herein, we developed a class of photoactive units based on the classic aldehyde-hydrazone moiety by conjugating several fluorescent aldehydes with various substituted phenylhydrazines. The resulting hydrazone-based photocages degraded upon exposure to light (365-450 nm), releasing fluorescent aldehydes. Fluorescent enhancements, redshifts or blueshifts were clearly observed during uncaging. For bio-application, morpholine-hydrazone based hybrid **BW3MP**, *staurosporine*-derived hybrids **BW3STS** and **FY4STS** were constructed. They exhibited high release efficiencies of MP (75.5%, **BW3MP**) and **STSA** (65.3%, **BW3STS**), respectively. **BW3MP** co-localized with a lysosome dye, exhibiting a Pearson correlation coefficient of 0.94. The biological activity of **BW3STS** was unmasked under irradiation, with a 4-fold increase in IC_{50}. Our work developed photoactive units that hold significant promise for the constitution of general suitable drug delivery systems (DDSs).

Photocages have garnered significant attention owing to their ability to precisely control the spatiotemporal release of functional entities, thereby enabling non-invasive modulation of biological processes and activities[1]. The core of photocage design lies in the photoactive units, which undergo structural changes upon exposure to light, thereby "unlocking" or activating the target molecules. Typical photoactive units, including *o*-nitrobenzyl derivatives[2], coumarin derivatives[3], BODIPY[4], xanthene derivatives[5], and others[6–8], have been developed to construct photocages with promising applications in bioimaging[9], drug delivery[10], and the manipulation of cellular processes[11]. Most of these photoactive units reported focus on improving uncaging performance with high efficiency, increasing water solubility, long wavelength irradiation, and stability, etc. via frequently used modification strategies including hydrophilic substituents[12], D-A (Donor-Acceptor) regulation[13], the incorporation of electrostatic interactions[14], and the selection of different groups to improve photolytic efficiency[15].

However, the development of photoactive units to enrich the structural diversity of photocages remains crucial[16]. Thus, great efforts have been devoted to developing photoactive units. For instance, Chen et al.[6] reported the construction of a multi-organelle-targeting and function-activatable fluorescent probe, Sanger-Mito/Lys/ER, based on a photocage derived from Sanger's reagent. Chaudhuri[17] reported a bimane-based photocage that enables release of carboxylic and amino acids. Sebej[18] discussed the use of fluorescein analog photoactive units, allowing for the controlled release. Situ et al.[19] explored Blebbistatin (Bleb) photocage, capable of precisely releasing halogen ions. A fluorescent organic nanoparticle for the delivery of two anticancer drugs was developed by Ray's group[20]. In addition, Wei et al.[21] reported the development of photolabile compounds derived from Sanger's reagent that cleave amide bonds upon photocleavage. Then, Zhou et al.[22] developed a photocage called photoactivatable nanobody conjugate inducers of dimerization (PANCIDs). Although these studies have expanded the structural library of photoactive units, most of the mentioned scaffolds of fluorescent molecules are still limited to some specific structures. Therefore, a universal photocage design strategy, founded on

[1]Fujian Provincial Key Laboratory of Screening for Novel Microbial Products, Fujian Institute of Microbiology, Fuzhou, Fujian, PR China. [2]Department of Pharmacy, Fujian Medical University Union Hospital, Fuzhou, Fujian, PR China. [3]The School of Pharmacy, Fujian Medical University, Fuzhou, Fujian, PR China. [4]College of Life Sciences, Fujian Agriculture and Forestry University, Fuzhou, Fujian, PR China. [5]Fujian-Taiwan-Hong Kong-Macao Science and Technology Cooperation Base of Intelligent Pharmaceutics, College of Material and Chemical Engineering, Minjiang University, Fuzhou, Fujian, PR China. [6]These authors contributed equally: Xia Wang, Jingming Zhou, Yu Cheng. [7]These authors jointly supervised this work: Yusheng Lu, Hongqiang Qiu, Lijun Xie. ✉e-mail: lu_yu_sheng@126.com; hongqiangqiu@fjmu.edu.cn; Lijunxie8224@outlook.com

innovative photoactive units compatible with a broad range of substrates, is urgently required to unlock the full potential of photocages in bio-applications[23].

Herein, inspired from the hydrazone-based photosensors[24] and oxime unit developed as a photoactive tag[15], we hypothesized that hydrazones may have the potential for development as a general photoactive unit. Thereafter, we successfully developed five series of hydrazone photocages via a one-step reaction between phenylhydrazine derivatives and various aldehydes of dyes. These compounds exhibited photodegradation upon visible light irradiation, reinstating the intermolecular charge transfer (ICT) effect and restoring fluorescence of aldehydes. These uncaging processes were fully confirmed by ultra-performance liquid chromatography-tandem mass spectrometry (UPLC-MS) and cellular confocal imaging.

To further demonstrate the versatility of hydrazone-based photocages in biomedical applications, we designed and synthesized compounds **BW3MP, FY4STS**, and **BW3STS** by incorporating the 3-(4-morpholinyl)-1-propylamine moiety and the *staurosporine* derivative to the aldehyde-hydrazone framework. The designed **BW3MP, FY4STS**, and **BW3STS** could serve as carriers of functional molecules, enabling the controlled release of fluorophore and bioactive agents. Among them**, BW3STS**, using **BW3** as a drug carrier, exhibited lower cytotoxicity and fluorescence intensity. Under 405 nm light irradiation, it decomposed to release **STSA** with an efficiency of 65.3%, restoring cytotoxicity against cancer cells, accompanied with fluorescent intensity significantly enhanced, thus achieving the visualized release of the drug.

Results

Design of hydrazone-based photocages

These photocages designed were shown in Fig.1a. We have chosen different aldehydes of dyes and phenylhydrazines to construct five series of photocages (**PC1-2, FY1-4, CM1-3, TP1-2, BW1-3**), which were synthesized by one-step reactions at room temperature. These aromatic aldehydes have excellent fluorescent properties[25–28], and the phenylhydrazone moiety served as a fluorescence-quenched tag, locked in an off-state until triggered by light to release their corresponding fluorophore (Fig.1a).

Next, we apply hydrazone-based unit for sub-organelle targeting, providing a foundation for targeted release in the future. **BW3MP** was synthesized by incorporating the 3-(4-morpholinyl)-1-propylamine moiety to the hydrazone framework (Fig.1b). Subsequently, **BW3MP** was investigated as a lysosome dye to validate its sub-organelle imaging.

Staurosporine, a natural alkaloid, has been recognized for its role in cancer treatment[29,30]. However, *staurosporine* has been excluded from potential clinical applications due to its lack of specificity[31]. Using *staurosporine* derivative (**STSA**) as a cargo to conjugate with hydrazone framework, we modified **BW3** and **FY4** respectively, resulting in **FY4STS**, and **BW3STS** as prodrugs of *staurosporine* (Fig.1b).

Uncaging process investigation

Absorption and emission analysis. It is known that hydrazones are inherently unstable under acidic conditions, undergoing hydrolysis to produce corresponding aldehydes[32]. Thereby, we firstly evaluated the pH stability of the **PC1, FY1, CM1, CM2, CM3**, and **BW1**. As shown in Supplementary Fig. 1, no hydrolysis or decomposition was observed at pH 1.2 and pH 7.4 in the absence of light, even after prolonged incubation (10 h), demonstrating good chemical stability of these compounds.

After that, the photolysis behaviors were monitored for targets under *UV-Vis* light irradiation by detecting the changes of their absorption spectra. As shown in Fig. 2a–d and Supplementary Fig. 2, the absorption bands of these compounds in DMSO all decreased during the uncaging, and the absorption bands of them gradually blueshifted to that of their corresponding aldehyde. These phenomena were consistent with the calculated results that the energy gaps (E_g) between Highest Occupied Molecular Orbital (HOMO) and Lowest Unoccupied Molecular Orbital (LUMO) for **PCA** (2.81 eV), **FYA** (3.19 eV), **TPEA** (3.53 eV) and **BWA** (3.42 eV) were slightly larger than those for **PC, FY, BW** and **TP** compounds (Supplementary Fig. 3 and Table S3). What is more, the absorption bands of **PC, FY**, and **BW** split into multiple characteristic absorption bands due to the presence of fully conjugated multiple phenyl rings in the aldehydes[33] (Fig. 2b–d). These observations may suggest the occurrence of uncaging reaction, leading to the generation of the substrate aldehyde.

Exceptionally, for compounds **CMA** and **CM1-3**, their absorptions of λ_{max} are almost identical (Fig. 2e and Supplementary Fig. 2). Notably, the absorption λ_{max} of **CM2** was not consistent with the calculated E_g of HOMO/LUMO. The transition from HOMO to LUMO in **CM2**, with E_g of 2.42 eV, was forbidden (Table S2 and Fig. 2f, $f = 0.014$, 99.3% of $S_0 \rightarrow S_1$). The predominant transition originated from the $S_0 \rightarrow S_4$ transition ($f = 1.492$), which was corresponding to the transition from the HOMO to the LUMO + 1 energy levels (Fig. 2f, 98.0%), with E_g of 3.39 eV (371 nm). Such a transition was in proximity to the absorption λ_{max} of **CM2** (385 nm).

Molar absorption coefficients (ε) of a range of compounds were determined to assess their photon absorption capability at specific irradiation wavelengths (Table 1). These results showed strong light absorption capabilities due to their large conjugated planes[34], allowing for efficient harvesting of photonic energy from light. Among them, the CM series exhibited the highest molar absorption coefficients of 3.21×10^4 L·mol^{-1}·cm^{-1} (**CM2**). In contrast, the **FY** series demonstrated the lowest values with a level of ~0.24×10^4 L·mol^{-1}·cm^{-1} as shown in Tables 1 and S3.

The photoluminescence (PL) fluorescence spectra are shown in Fig. 3 and Supplementary Fig. 4. Interestingly, despite the high ε of these compounds, their fluorescence intensity is relatively weak as compared with their corresponding substrate aldehyde. After uncaging, their noticeable fluorescent intensities enhancement, ranging from 6.5 to 20.3 folds of initial points could be observed with all the compounds except **CM1**. Among them, compounds of **PC, FY**, and **CM** series showed no significant shift in the maximum emission wavelength after uncaging process. The **BW** and **TP** series initially exhibited green or blue fluorescence emission. After uncaging, the emission spectra significantly blueshifted, with notably enhanced fluorescence intensity (e.g., 8.5 times for **BW3**, 13.5 times for **TP2**). The weak fluorescence of them was mainly attributed to the blockage of the intramolecular charge transfer (ICT) effect in the targets. Specifically, the substrate aldehyde emits fluorescence via the ICT effect. When additional functional groups are introduced, the ICT state becomes suppressed, causing energy dissipation through non-radiative transitions. After deprotection (cage removal), the ICT state is restored, thereby recovering their original fluorescence, which closely resembles that of their corresponding substrate aldehydes (Supplementary Fig. 5).

In case of compounds **FY4** and **BW3** with two conjugated planes, calculations of their excited state (in Fig. 3c and Supplementary Fig. 6) might suggest that the occurrence of a Twisted Intramolecular Charge Transfer (TICT) effect between two planes caused the fluorescence quenching[35]. For **FY4**, when a molecule returned from the excited state (S_1) to the ground state (S_0), a portion of the energy was consumed for molecular torsion, which resulted in vibrational relaxation, leading to energy loss. The calculated dihedral angle of **FY4** changed from 38.21° to 61.43° upon transitioning from S_1 to S_0, as shown in Fig. 3c. Differently, the atoms of **CM1** and **CM2** were almost distributed within the same plane under the S_1 and S_0 states, so that the initial fluorescence of **CM1** was relatively strong (Fig. 3d). However, the initial fluorescence of **CM2** was very weak (Fig. 3e). The fluorescence quenching of **CM2** might be due to a donor-excited photo-induced electron transfer (*d*-PET) effect (Fig. 3f) as well as **TP2** and **PC2** (Fig. 3g, h). These three targets are with electron-withdrawing groups (-NO_2) on the benzene rings as electron acceptors. Taken **PC2** as an example, the LUMO energy level of acceptor was situated between the HOMO and LUMO energy levels of the electron donor. The electron transferred to the electron acceptor so that it did not undergo a radiative transition (Fig. 3i).

UPLC-MS analysis. The solid evidence for confirming the uncaging processes was further provided by UPLC-MS, where we extracted the ion

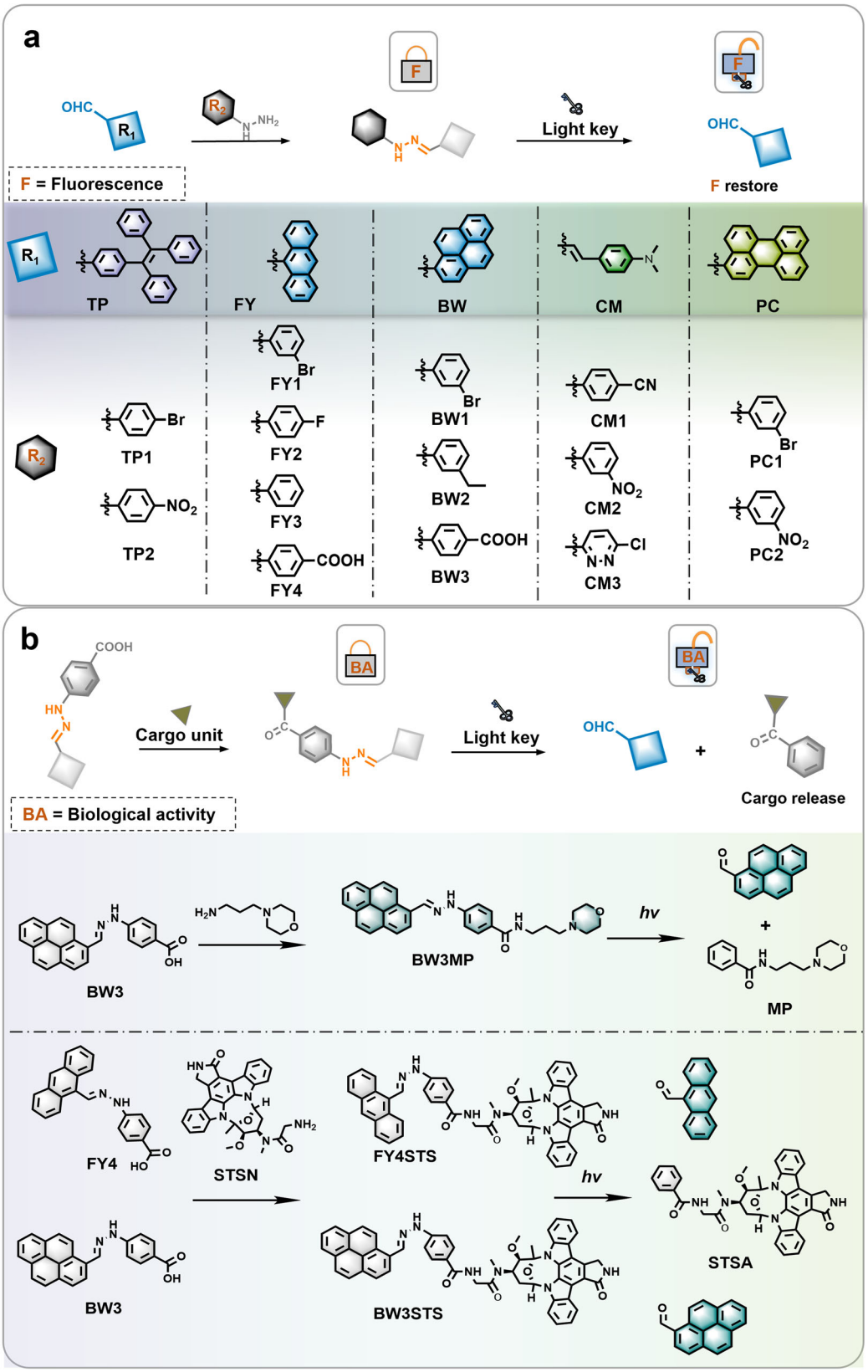

Fig. 1 | Design of five series hydrazone-based photocages. a The photocages synthesized by one-step reactions and triggered by light to release their corresponding fluorophore, **b** design of BW3MP as a sub-organelle imaging tool, and design of **FY4STS** and **BW3STS** as prodrugs.

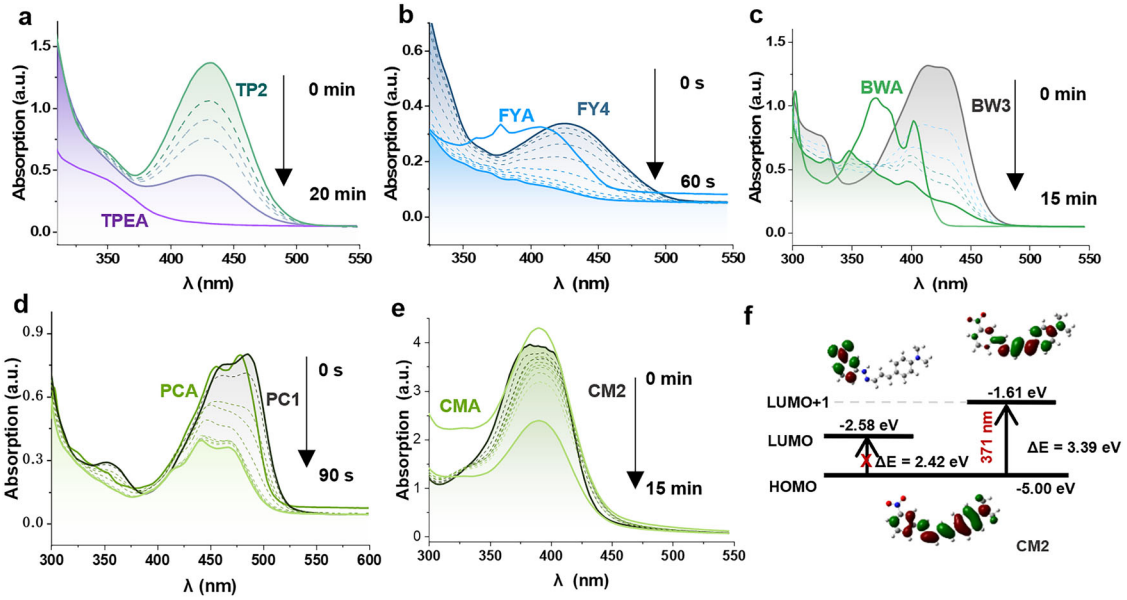

Fig. 2 | The changes in absorbance of the photocages. a–e The absorbance of **TP2**, **FY4**, **BW3**, **PC1**, **CM2** (10 μM in DMSO, dark curves: initial absorption spectra, dashed curves: intermediate time spectra, light colored solid lines without tag: spectra at specific time points indicated on the right) over time under light irradiation compared to the absorbance of their related aldehydes **TPEA**, **FYA**, **BWA**, **PCA** and **CMA** (10 μM in DMSO, light colored solid lines with compound tag), **f** Frontier molecular orbital energy levels and electron density of HOMO/LUMO of CM2.

currents of the targets and the corresponding substrate aldehyde. Without exception, as the irradiation continued, the ion current of the targets gradually decreased until it disappeared, while the ion current of the substrate aldehyde gradually increased (Supplementary Figs. 7 and 8). These changes, together with the changes in the absorption (Fig. 2a–e and Supplementary Fig. 2) and emission spectra (Fig. 3 and Supplementary Fig. 4), unequivocally confirmed the realization of the degradation of hydrazones to aldehydes. In addition, the hydrazone degradation and aldehyde release quantum yield of them were listed in Table 1, indicating they could be efficiently utilized to trigger photoreactions, resulting in their uncaged processes. Notably, the uncaging products were fundamentally distinct from the conventional photoisomerization behavior of hydrazone-based photoswitches reported before[36].

The properties of BW3MP and its photoreaction mechanism. We modified **BW3** by attaching a morpholine unit to yield **BW3MP**. The photodegradation processes of **BW3MP** were also confirmed using fluorescence spectroscopy and UPLC-MS. After uncaging, the changes in absorption and emission spectra of **BW3MP** were similar to those of **BW3**, with the absorption spectra showing blue-shift and attenuation and the emission spectra exhibiting blue-shift and enhancement (Fig. 4a–c). Both **BW3** and **BW3MP** underwent partial fluorescence quenching due to the blockage of the original ICT of **BWA**. However, quantum mechanical calculations revealed that the **BW3** exhibited a tilted conformation (Fig. 4d), with the pyrene and the carboxyphenyl groups forming an angle, whereas the **BW3MP** displayed a nearly coplanar conformation between these two moieties (Fig. 4e). As a result, unlike the TICT quenching that was observed in **BW3, BW3MP** exhibited an *a*-PET effect (Fig. 4f), where the electron transitions between the Donor and Acceptor were existed[37].

Subsequently, the uncaging mechanism of hydrazone-based photocages was also investigated, taking **BW3MP** as an example. Upon irradiation, **BW3MP** underwent isomerization, which may be based on the *Z*/*E* configuration transformation (step 1 in Fig. 5d), previously reported by Zhang et al.[38]. As shown in Fig. 5f, the ion peaks of *N*-(3-morpholinopropyl) benzamide (**MP**) **and BWA** gradually intensified, while the **BW3MP** peak weakened, implying that Step 1 (isomerization) and Step 2 (degradation) occur simultaneously. Notably, the **BW3MP** peak declined faster than its isomer, suggesting that **BW3MP** itself (rather than its isomer) predominantly participates in the degradation pathway. Next, the mass spectrometry captured a clear $[M + 2O + H]^+$ of *m*/*z* 523.2323 at Rt = 2.6 min (Fig. 5f), indicating the involvement of oxygen. Thereafter, we also observed that **BW3MP** underwent almost no degradation and only exhibited isomerization under oxygen-free environment (Fig. 5a and Supplementary Fig. 9a), with the intensity of absorption and emission spectra slightly reducing (Supplementary Fig. 9b, c). The similar phenomena of some others were shown in Supplementary Fig. 10. Moreover, ROS detection in **BW3MP** using the DCFH-DA probe revealed a significant fluorescence enhancement under light irradiation (Fig. 5b), attributable to the irreversible oxidation of the probe by accumulated ROS. Notably, while the fluorescence signal continuously rises due to the irreversible nature of the probe's oxidation, the actual ROS generation rate in the system may decrease as **BW3MP** is consumed during the reaction. In contrast, no notable fluorescence increase of DCFH-DA was observed in the dark, confirming the light-dependent generation of ROS by **BW3MP**. Based on these observations and similar mechanism reported by Han's group[15], we proposed a photo-oxidation process involving ROS (step 3). $^1O_2$ exhibited nucleophilic reactivity, preferentially targeting the N-H position, which possessed the highest positive electrostatic potential from quantum mechanical calculations (Fig. 5c and Supplementary Fig. 3). Additionally, unlike the hydrolysis process, the photodegradation products were MP and **BWA** (Fig. 5d, f).

Table 1 | Photophysical data of the compounds

	λ (nm)	ε (10^4L/(mol·cm))	Excited State	*f*	E_g (eV)	Φ_u ($\times10^{-3}$)	Φ_d ($\times10^{-4}$)
TP2	365	1.38	$S_0 \rightarrow S_5$	0.7805	2.83	3.34	4.91
FY4	405	0.21	$S_0 \rightarrow S_2$	0.2416	3.67	287	202
BW3	385	1.70	$S_0 \rightarrow S_3$	0.8242	3.03	16.6	23.2
CM2	365	3.21	$S_0 \rightarrow S_4$	1.4917	2.88	1.49	4.32
PC1	450	2.65	$S_0 \rightarrow S_1$	0.5140	2.17	1.61	3.64

λ irradiation wavelength, ε molar absorption coefficients calculated at the absorption λ_{max} of each compounds (TP2 at 430 nm, FY4 at 428 nm, BW3 at 414 nm, CM2 at 386 nm, PC1 at 494 nm), *f* oscillator strengths, E_g energy gap between HOMO and LUMO, Φ_u quantum yield of hydrazone degradation, Φ_d quantum yield of aldehyde release.

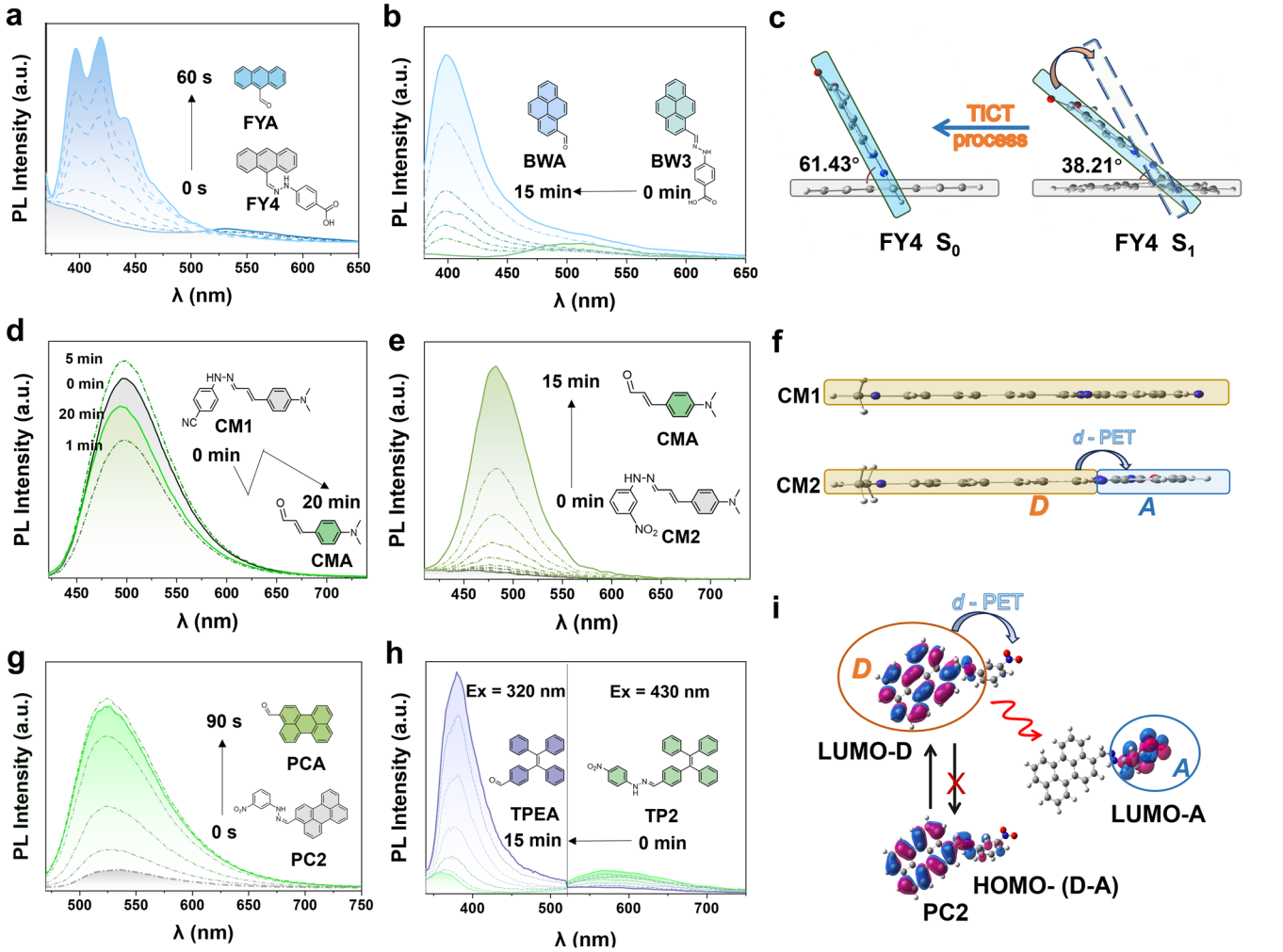

Fig. 3 | PL spectra of major compounds for different irradiation times. Gray curves: initial emission spectra; dashed: emission spectra at intermediate time points; colored solid lines: spectra at specific time points indicated on the right. **a FY4** with 169.5 mW·cm^{-2} at 405 nm irradiation, λ_{ex} = 365 nm, **b BW3** with 166.0 mW·cm^{-2} at 385 nm irradiation, λ_{ex} = 365 nm, **c** Dihedral angle changes between the benzene ring and anthracene ring in S_0/S_1 of **FY4**, and the TICT effect of **FY4**, **d**, **e CM1** and **CM2** with 164.3 mW·cm^{-2} at 365 nm irradiation, λ_{ex} = 385 nm, **f** Comparative analysis of fluorescence mechanisms in CM1 and **CM2**, D: electron donor, A: electron acceptor, **g PC2** with 171.2 mW·cm^{-2} at 450 nm irradiation, λ_{ex} = 460 nm, **h TP2** with 164.3 mW·cm^{-2} at 365 nm irradiation, λ_{ex} = 320 and 430 nm, **i** Frontier molecular orbital energy levels and electron density distributions of HOMO/LUMO for **PC2**, along with the *d*-PET effect of **PC2**.

Figure 5d displays the time-dependent ^{1}H NMR evolution of **BW3MP** (1.5 mM in DMSO-d_6) under irradiation, with direct comparisons to **BWA** and **MP**. **BW3MP**-specific proton signals (highlighted in purple boxes) progressively diminish with irradiation time, most notably the hydrazone N-H proton signal at 10.9 ppm, indicative of bond cleavage. Concurrently, characteristic proton signals of **BWA** and **MP** characteristic proton signals (marked by green and red boxes) intensify, confirming they were photodegradation products. Unassigned peaks in Fig. 5g likely originate from **BW3MP** isomer. Notably, the **MP** release rate of **BW3MP** was calculated to be 75.5% (Fig. 5g), which suggested that **BW3MP** could serve as visualizable photocages for the release of fluorophore and small molecules. Based on the computational results and experimental observations, we proposed the reaction mechanism as depicted in Fig. 5d, where $^1O_2$ initially attacked the N-H (step 4), followed by [O-O-H] attacking the C=N bond from the other side (step 5), forming a peroxide intermediate. Subsequently, the compounds decomposed to release the aldehyde, forming an unstable intermediate with N≡N$^+$- (step 6), and finally decomposed to release N_2 (step 7).

Application for cell imaging and precise sub-organelle visualization

Confocal imaging of cells. Hydrazone units have been widely applied as key intermediates, linker of ADC drugs[39] or pharmacophores in drug development[40], fluorescent probes[41], and molecular sensors[42]. In CCK-8 assay, the high cell viability was observed under either light or dark conditions, indicating that the photocages and their photoreaction products did not exhibit obvious cytotoxicity (Supplementary Fig. 11), which piqued our interest in designing low-damage cellular tools using these photocages. Next, MCF-7 cells were utilized for bioimaging investigation (Fig. 6a–d and Supplementary Figs. 12–14). In the case of **BW3**, fluorescence in cells showed significantly red-shifted under 405 nm excitation (Fig. 6a, b), while **BW3** maintained its original fluorescence without irradiation (Fig. 6c, d). In addition, the fluorescence of **BW3** could be maintained for no less than 10 min without decay, which may be an advantage over traditional dyes with quenched effect. Notably, **BW3**'s initial point image showed relatively high fluorescence intensity, which was distinctly different from their change of emission spectra. The phenomenon may be explained by the environmentally sensitive of TICT effect[43]. The cytoplasm, having a higher viscosity, hindered their planar rotation process, thereby partially obstructing TICT, which allowed for partial recovery of the fluorescence (Fig. 6f). Similarly, TICT effect of **FY4** was also suppressed in cells, so that **FY4** has a blue light emission at 0 s (Supplementary Fig. 9b). In contrast, **TP2, PC1**, and **CM2**, which based on PET quenching effect, were week emission and enhanced under irradiation in MCF-7 cells (Supplementary Figs. 9a, c, d and 14), which

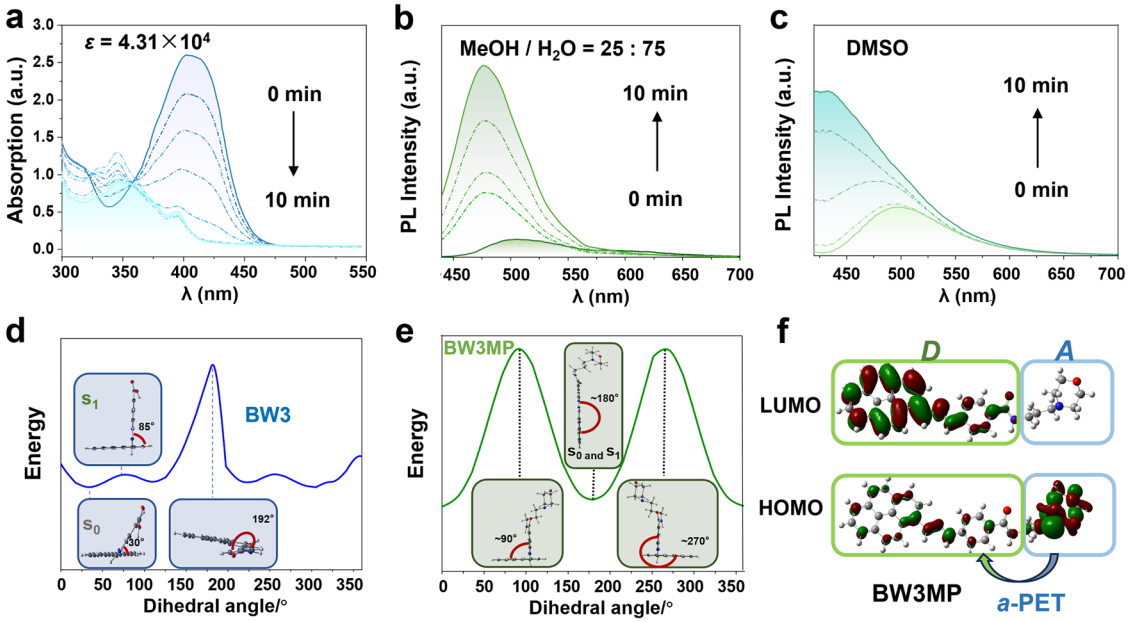

Fig. 4 | The properties of BW3MP. a Absorption spectra of **BW3MP**, where ε is the molar absorption coefficient, **b**, **c** Emission spectra of **BW3MP** in MeOH/H_2O (25:75) and DMSO solution with 82.3 mW·cm^{-2} at 405 nm irradiation, λ_{ex} = 410 nm. The dihedral angle changing and their energy of **BW3** (**d**) and **BW3MP** (**e**). In both the S_0 and S_1 states of **BW3MP**, the pyrene and benzene rings remain coplanar (as calculated using Gaussian 09 software with IRC analysis at a step size of 6°). **f** *a*-PET effect of **BW3MP**.

were in good agreement with the respective changes of PL spectra in DMSO, respectively. One the other hand, uncaged **BW3** exhibited green emission in cells, which was different from the blue light emission in PL. It might be caused by typical excimer emission of **BWA** due to dimer formation in aqueous environment[27]. One piece of evidence was that **BWA** itself also emits green light in cell imaging (Supplementary Fig. 13). Another was that uncaged **BW3** in MeOH/H_2O emits a cyan light at 475 nm, which is longer wavelength than that in DMSO (Supplementary Fig. 5c and Fig. 6f). These phenomena are similar to the uncaging process of **BW3MP** (Fig. 4b). **BW3MP** initially emitted a bright cyan light in the cell images (Fig. 6e). During the uncaging process, the blue light gradually diminished, the green light remained constant, and there was a slight increase in red channel. The overlayed images showed the transition of luminescence from blue to green (Fig. 6g, h).

Sub-organelle localization. As a demonstration of its application, **BW3MP** was selected for sub-organelle localization. A red lysosomal dye called Lyso-Tracker Red (C1046) was used to stain cells, serving to label the lysosomes within the cells, and then **BW3MP** was added to co-stain (Fig. 7a–d). As shown in Fig. 7a, b, we also observed the similar phenomenon of diminishing intensity at blue channel and enhanced red light. The faint red light at initial point in the red channel originates from Lyso-Tracker Red, while the blank control **BW3MP** almost did not emit red light at initial point (Figs. 5d and 7a). Through Pearson correlation coefficient analysis, a correlation coefficient of 0.94 was achieved between the location stained by the lysosomal dye and the position of **BW3MP** in the blue channel at starting time point. (Fig. 7c, d), which suggested that **BW3MP** and the dye were co-localized very well. The experimental results indicated that **BW3MP** may have the potential to serve as a fluorescent probe for lysosome targeting and dynamic visualization imaging.

Application for drug release

Drug release of STSA. The efficient release of small molecules has sparked our further interest in designing hydrazone-based prodrugs. Two hybrids **BW3STS** and **FY4STS** were designed and synthesized by attaching *staurosporine* derivatives via one-step modification. As was shown in Fig. 8a, b, **BW3STS** exhibited an emission peak at 520 nm and an absorption peak at 420 nm. **BW3STS** followed a fluorescence quenching process driven by *a*-PET effect, which accounts for its initially weak fluorescence (Fig. 8d). As the irradiation time increases, both the absorption peak at 420 nm and the emission peak at 520 nm diminish to nearly disappearance, while the emission peak at 400 nm shows a significant enhancement. Additionally, we observed a gradual decrease in the **BW3STS** peak at *m*/*z* 870 (Rt = 4.7 min) in MS spectra, along with increases in the molecular ion peaks at 231 and 628 (Rt = 3.8 min), which correspond to the photodegradation products **BWA** and **STSA** (Supplementary Fig. 15). The release of **BWA** is mainly responsible for the notable increase in fluorescence. Similar phenomenon can also be observed in the photodegradation of **FY4STS** (Supplementary Figs. 16–18). The multiple peaks in the emission spectra during uncaging of **FY4STS** (Supplementary Fig. 16a) were similar to those observed for **FYA** (Fig. 3a), suggesting that the main emitter is likely to be **FYA**. Notably, the photodegradation yield of **STSA** reaches 65.3% (Fig. 8c) with **BW3STS** and 45.3% with **FY4STS** (Supplementary Fig. 16c).

Then, we visually observed the release of **BW3STS** in cells. **STSA** itself has high toxicity in cells, with an IC_{50} of 0.9 ± 0.20 μM, while **BW3STS** demonstrated low toxicity in cells, with an IC_{50} of 17.2 ± 3.57 μM under non-irradiation conditions. Particularly, there was no significant toxicity to MCF-7 cells within the dosage range of 0–5 μM, indicating that **BW3STS** as a prodrug indeed can "cage" the toxicity of **STSA**. After 30 min irradiation, the toxicity increased 4-fold, with an IC_{50} reaching 4.8 ± 0.34 μM (Fig. 8e). This comparison also indicates that the drug was released under light and exhibited more pronounced biological activity. Cellular imaging allowed us to visualize the release process of **BW3STS**. Initially, the cell morphology was intact (in Fig. 8f), with clear outlines and exhibiting cyan fluorescence, suggesting that **BW3STS** has weak toxicity, while the fluorescence gradually shifted to yellow and intensified. The degradation process of **FY4STS** also accompanied similar phenomena of fluorescence enhancement and apoptosis in cells (Supplementary Fig. 17). These results suggest that hydrazone can be employed for the design as a linker, allowing for controllable, visualized, and efficient release of the biologically active **STSA**.

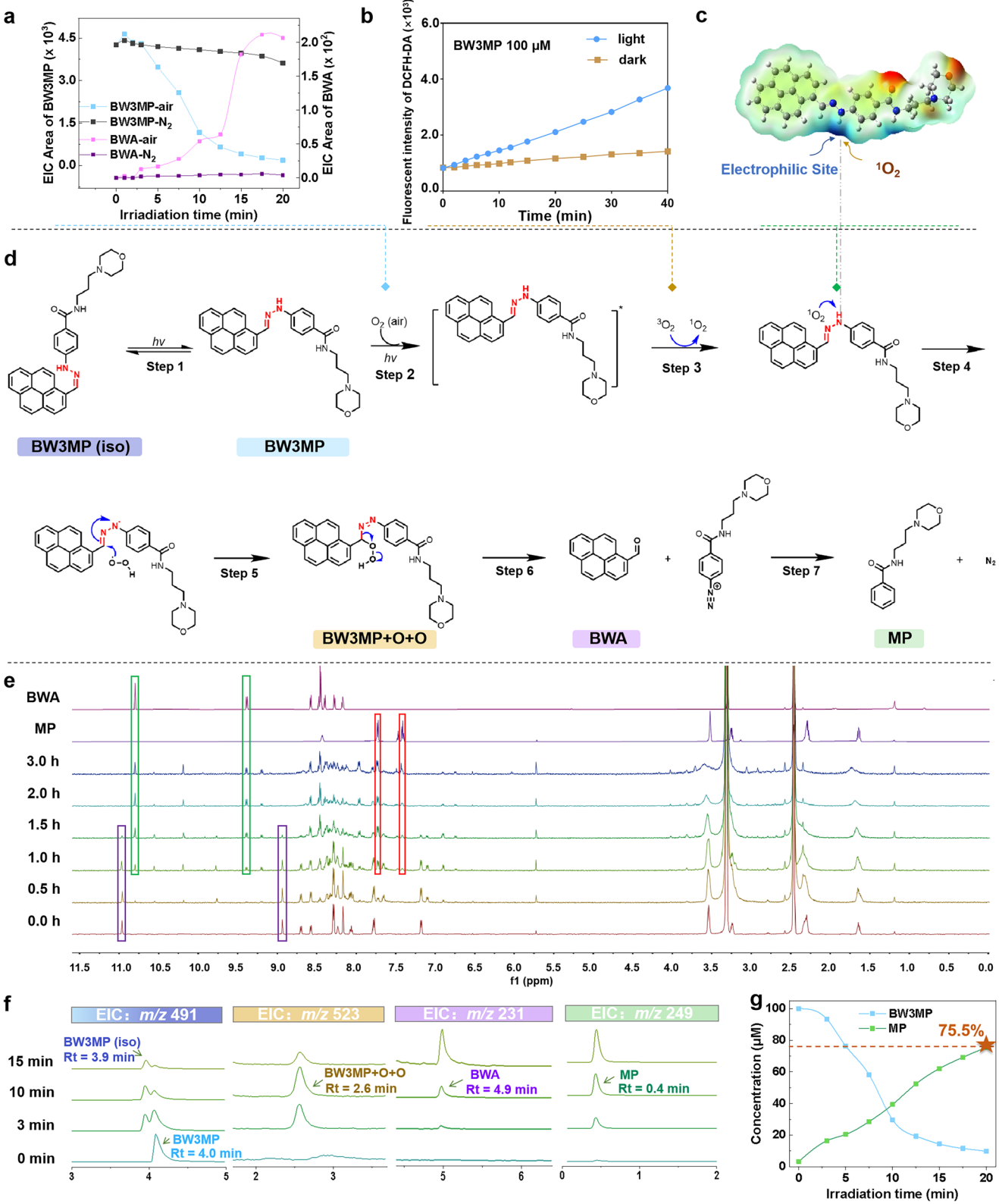

Fig. 5 | Photoreaction mechanism of photocages taking BW3MP as an example. **a** Mass spectra peak area under air environments and oxygen-free environment, **b** Relative ROS levels of **BW3MP** (100 μM in DMSO, detected by fluorescence intensity of DCFH-DA fluorescent probe) with irradiation and non-irradiation, **c** Electron density of **BW3MP**, **d** The proposed uncaging mechanism for **BW3MP**, **e** Comparison of ^{1}H NMR changes in **BW3MP** (1.5 mM in DMSO) during photodegradation with ^{1}H NMR of **BWA** and **MP**. **f** EIC analysis of **BW3MP** and its uncaged products under different irradiation times, **g** Conversion rate of **BW3MP**, **MP** release rate was 75.5%.

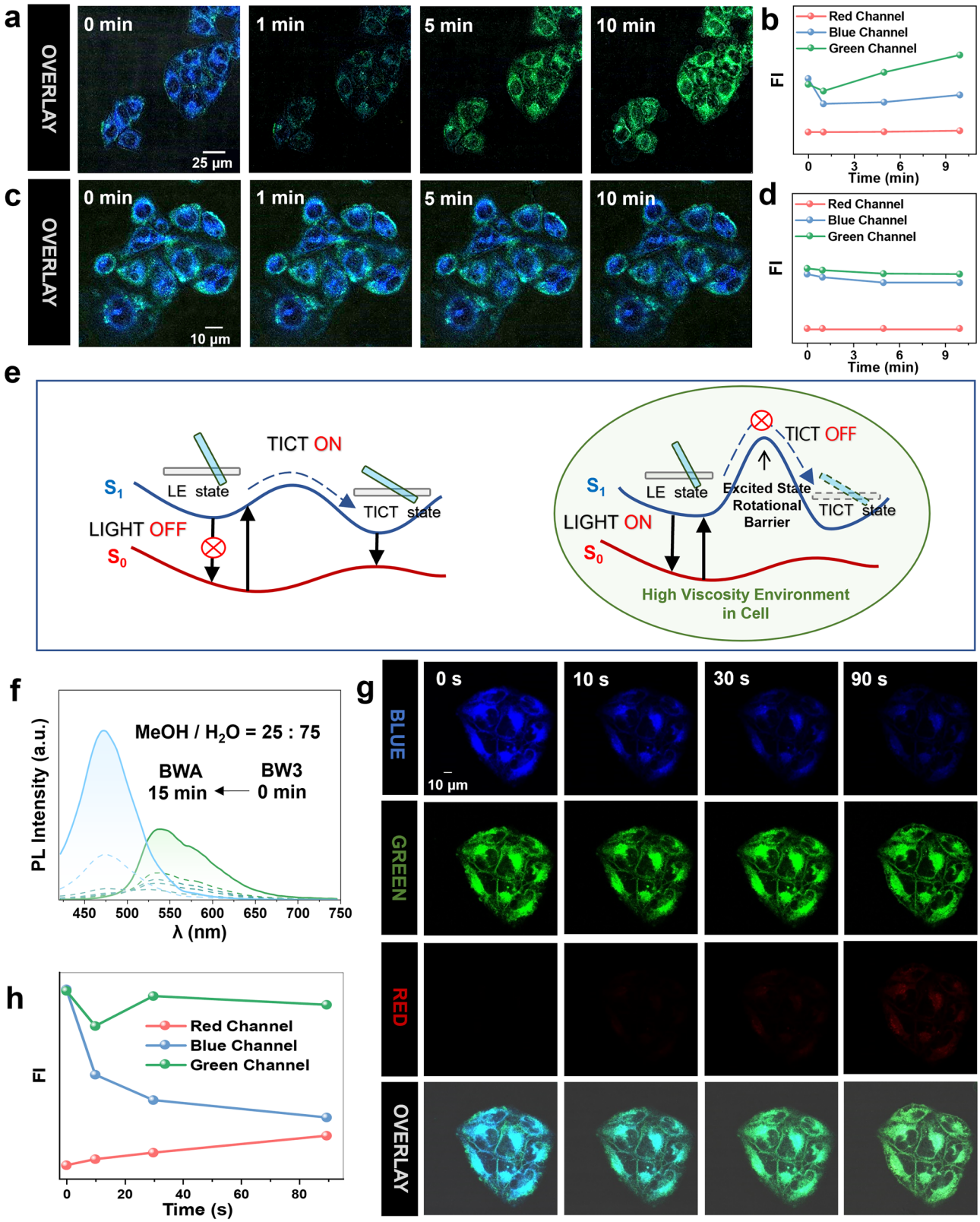

Fig. 6 | Confocal imaging of cells treated with BW3 and BW3MP. a Confocal imaging of cells treated with **BW3** under irradiation. Overlay of four channels: red, blue, green and bright field cellular image (405 nm laser irradiation), **b** Fluorescence intensity (FI) changes across channels under irradiation, **c** Confocal imaging of MCF-7 cells treated with BW3 without irradiation Overlay of four channels: red, blue, green and bright field cellular image, **d** FI changes across channels without irradiation. **e** The TICT effect of **BW3**, and suppressed TICT in the intracellular environment. **f** PL spectra of **BW3** in MeOH/H_2O for different irradiation times (λ_{ex} = 365 nm). **g** Confocal imaging of cells with **BW3MP**: Overlay of four channels: red, blue, green, and bright field cellular image (405 nm laser irradiation). **h** The fluorescence intensity of three channels (red, blue, and green) in (**g**).

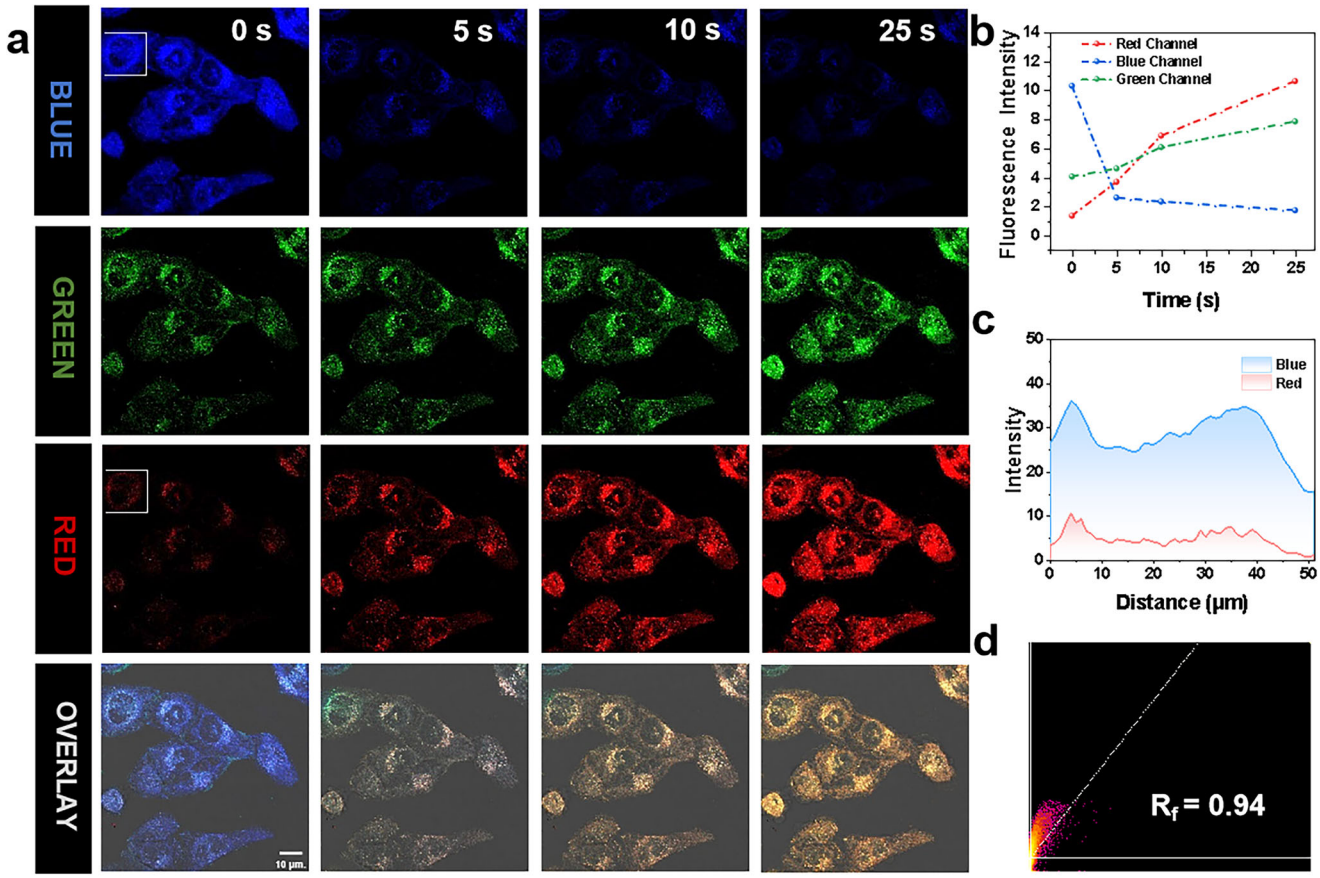

Fig. 7 | Colocalization of lysosomes using BW3MP, with Lyso-Tracker Red (C1046). a Confocal imaging of cells with **BW3MP** and Lyso-Tracker Red (C1046), overlay of four channels: red, blue, green and bright field cellular image (405 nm laser irradiation), **b** The fluorescence intensity of the three channels (red, blue and green), **c** Correlation analysis of the blue channel and red channel at 0 s in the white square regions, **d** The correlation coefficient between the location stained by the lysosomal dye and the position of **BW3MP** in the white square regions.

Discussion

In this study, we have developed a class of photocages with the aldehyde-hydrazone unit as a photoactive tag, where the hydrazone can be employed as a general tag to anchor with multiple aldehyde-based fluorescent probes. The majority of these hydrazone conjugates (**FY, CM, BW**, and **PC**) exhibited remarkable pH stability (pH 1.2-7.4), with degradation only upon light irradiation. Depending on the substituents, the fluorescence quenching of the caged compounds is based on various mechanisms such as TICT or PET, but the uncaging process of them released the fluorophore, restoring fluorescence, which is accompanied by evident phenomena such as redshifts, blueshifts, or enhancements in fluorescence. Next, we proposed that the photodegradation process follows a photo-oxidation reaction mechanism, as inferred from mass spectra results. Photolysis occurred more rapidly in aerobic environments, with the formation of a peroxide intermediate state during the process. The N-H bond was more susceptible to attack by O_2 in the excited state, as supported by quantum mechanical calculations. Moreover, the detection of distinct fluorescence signal changes indicated that these photocages could function as fluorescence probes, potentially offering superior fluorescence brightness compared to conventional dyes that are subject to fluorescence quenching[44].

Additionally, the hydrazone unit could be linked to a variety of bio-functional structure for different bio-applications. As a demonstration of their utility, **BW3MP, FY4STS**, and **BW3STS** successfully released fluorophores and small active molecules. Notably, the **MP** release rate of **BW3MP** was with high efficiency of 75.5%. Meanwhile, the **BWA** release rate was calculated about 25%, which may be due to the photo-instability of **BWA**[45], as it underwent decomposition. Moreover, **BW3MP** achieved co-localized with a commercial lysosome dye, exhibiting a Pearson correlation coefficient of 0.94, confirming its potential as a sub-organelle localizer. The designed **BW3STS** successfully "caged" the toxicity of the *staurosporine* derivative. Under light exposure, the anticancer activity of **BW3STS** was enhanced 4-fold. The *staurosporine* derivative were released through photodegradation of the hydrazone unit, restoring its biological activity, demonstrating its potential as a photocage prodrug.

In summary, we have confirmed the feasibility and universality of this photoactive unit, facilitating the release of a variety of aldehyde-based fluorescent groups. Further research will focus on fine-tuning the substituents of these photocages for near-infrared responsiveness and enhanced bio-accessibility. We envision that hydrazone-based photocages will emerge as a valuable platform for bioimaging, subcellular localization, and drug delivery, overcoming the challenges of insufficient drug release efficiency in approved hydrazone-based ADC drugs[46,47].

Methods

Materials

All starting materials were obtained from commercial suppliers and used without further purification. tetraphenylethylene aldehydes (**TPEA**), **PCA, CMA, BWA, FYA**, and the hydrazine and its derivatives used in the experiment were purchased from Accela ChemBio Co., Ltd. (China). Methanol was sourced from Xilong Scientific Co., Ltd. (China). Unless otherwise specified, all other reagents and solvents were of Analytical Reagent (AR) grade and were obtained from Shanghai Hushi Laboratory Equipment Co., Ltd. (China), used as received.

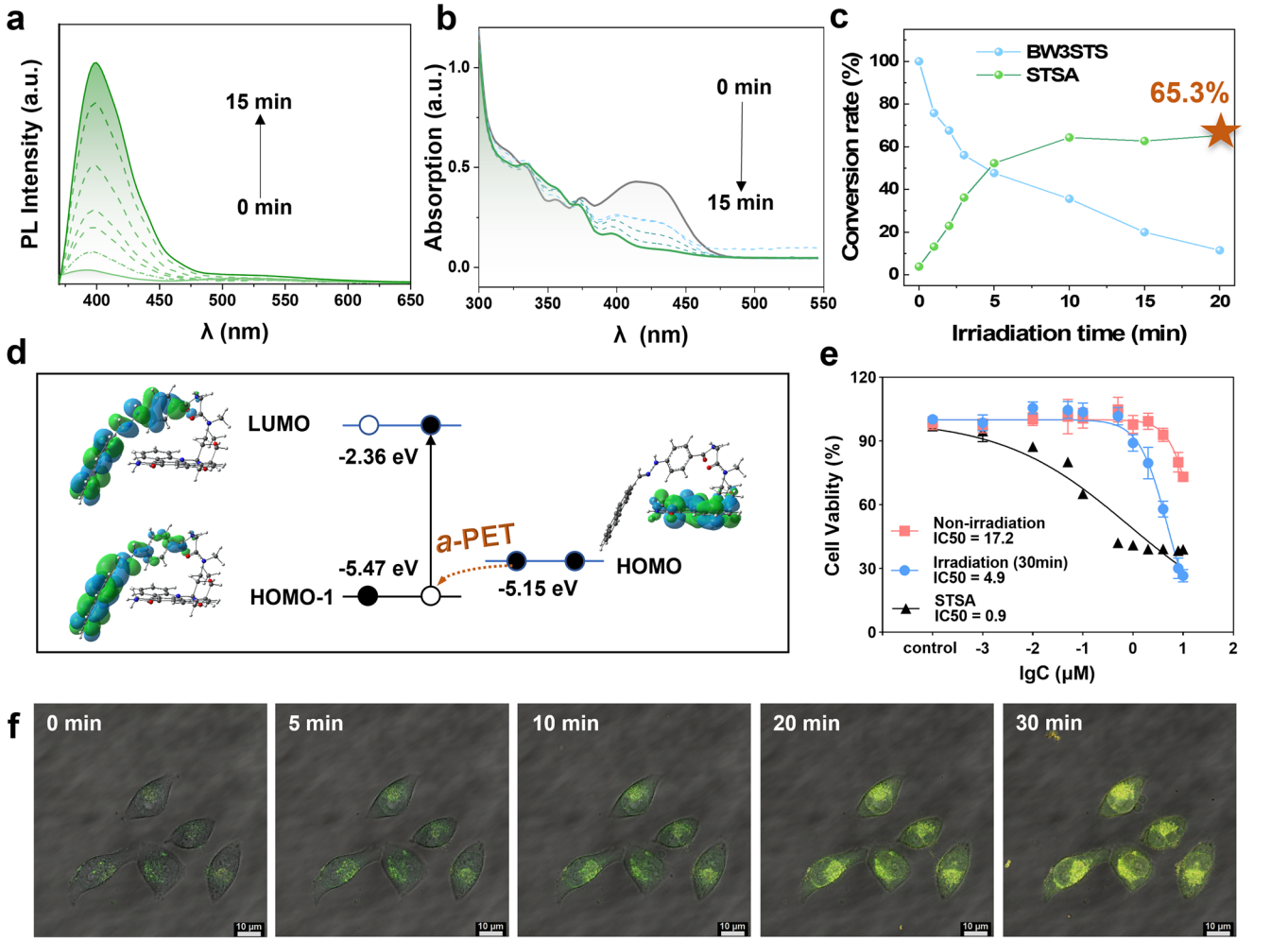

Fig. 8 | Photodegradation process of BW3STS prodrug. a Emission and **b** absorbance of **BW3STS** in photodegradation processes with 81.8 mW·cm^{-2} at 405 nm irradiation, λ_{ex} = 330 nm, **c** Conversion rate of **BW3STS**, and **STSA** release rate (65.3%) of **BW3STS**, **d** *d*-PET effect of **BW3STS**, **e** Cytotoxicity of **STSA** and **BW3STS** with irradiation and non-irradiation, error bars show cell viability of three independent measurements. **f** Confocal imaging with BW3STS. Overlay of four channels: red, blue, green, and bright field cellular image (laser irradiation: 120 mW·cm^{-2} intensity at 405 nm).

Thin-layer chromatography (TLC) and column chromatography

Reactions were magnetically stirred and monitored on a thin-layer chromatography (TLC) Silica gel 60 G254 plate from Shanghai Haohong Scientific Co., Ltd. The purification of compounds was performed with silica gel (200-300 mesh) column chromatography.

UPLC-MS

High-resolution mass spectra (HRMS) were obtained at the Mass Spectrometry Service Center of Fujian Institute of Microbiology on an Agilent 6545 Q-TOF LC-MS.

Synthesis

A mixture of aromatic aldehydes (2 mmol), any one of them, such as 9-anthre carboxaldehyde (**FYA**), 3-perylenecarboxaldehyde (**PCA**), cinnamaldehyde (**CMA**), 1-pyrenecarboxaldehyde (**BWA**) and TPE aldehydes (**TPEA**), was reacted with phenylhydrazine derivatives (6 mmol) in DCM solution (20 mL) and stirred in the nitrogen environment with proper reaction times under the protection from light. The crude products were purified by column chromatography on silica gel eluted with (DCM/MeOH = 15:1) to give the targets. The products were subsequently filtered, washed with DCM, and dried over anhydrous Na_2SO_4. All the steps of the synthesis were conducted at room temperature. The derivatives of 3-perylenecarboxaldehyde phenylhydrazone, 9-anthraldehyde phenylhydrazone, cinnamaldehyde hydrazone, 1-pyrenecarboxaldehyde hydrazone, and TPE aldehyde hydrazone were synthesized (Fig. 1a), which were named as **PC1-PC2, FY1-FY4, CM1-CM3, BW1-BW3**, and **TP1-TP2**, respectively. The HRMS results were shown in Figs. S1–S14 in Supplementary Data 4, and the NMR results were shown in Figs. S21–S48 in Supplementary Data 4.

The main synthetic method of **BW3MP** is as follows: 2 mmol of compound BW3, 1 mmol of EDCI, and 1 mmol of HOBt were dissolved in 10 mL of DCM, and then stirred at room temperature in the dark under the protection of nitrogen gas for 240 min, followed by the dropwise addition of 200 μL of 3-(4-Morpholino)-1-propylamine. For an additional 60 min, the reaction mixture was completed. The crude materials were filtered, washed with DCM, and dried over anhydrous Na_2SO_4. The HRMS results were shown in Fig. S15 in Supplementary Data 4, and the NMR results were shown in Figs. S49 and S50 in Supplementary Data 4.

To study the release rate, the reference compound MP was synthesized from benzoic anhydride and 3-(4-Morpholino)-1-propylamine as follows: 1 mmol of benzoic anhydride and 1 mmol of EDCI, and 1 mmol of HOBt were dissolved in 10 mL of DCM, and then stirred at room temperature in the dark under the protection of nitrogen gas for 240 min, followed by the dropwise addition of 200 μL of 3-(4-Morpholino)-1-propylamine. For an additional 60 min, the reaction mixture was completed. The crude materials were filtered, washed with DCM. The HRMS results were shown in Fig. S16 in Supplementary Data 4, and the NMR results were shown in Figs. S51 and S52 in Supplementary Data 4.

The obtained MP was diluted with DMSO to different concentrations to prepare the standard curve.

The main synthetic method of **BW3STS** and **FY4STS** is as follows: 2 mmol of compound **FY4** or **BW3**, 2 mmol of **STSN**, 1 mmol of HATU and 1 mmol of DIBG were dissolved in 10 mL of DCM, and then stirred at room temperature in the dark under the protection of nitrogen gas for no less than 240 min. The crude products were purified by column chromatography on silica gel eluted with (DCM/MeOH 15:1) to give the targets. **STSA** was synthesized with the similar way. The HRMS results were shown in Figs. S17–S20 in Supplementary Data 4, and the NMR results were shown in Figs. S53–S60 in Supplementary Data 4.

UV-Vis absorption and emission spectroscopy

UV-Vis absorption and Emission spectra, quantum yields, and all the fluorescence measurements were recorded using a Varioskan LUX 3020-80110.

Photochemical quantum yield determination

The quantum yield for the photoreaction of aldehyde-hydrazone cage was assessed in the following manner.

$$\Phi_u = \frac{\Delta M}{N_P} \tag{1}$$

$\Delta \boldsymbol{M}$ Number of *staurosporine* aldehyde molecules generated

$\boldsymbol{N_p}$ Number of absorbed photons

The calculation of the number of aldehyde molecules generated was carried out using Eq. 2.

$$\Delta M = \Delta c \cdot V \cdot N_A \tag{2}$$

$\boldsymbol{V}$ Irradiated volume

$\boldsymbol{N_A}$ Avogadro's number

$\Delta \boldsymbol{c}$ Concentration increases of the substrate aldehyde

The number of absorbed photons ($\boldsymbol{N_p}$) can be evaluated from the measured the optical power absorbed by the test solution ($\boldsymbol{P_a}$), irradiated time ($\Delta \boldsymbol{T}$) and the energy of a photon of 365 nm wavelength ($\boldsymbol{E_p}$) according to Eq. 3.

$$N_p = \frac{P_a \cdot \Delta T}{E_p} \tag{3}$$

$\boldsymbol{P_a}$ can be found by the following Eq. 4.

$$P_a = E_e \cdot S \cdot (1 - 10^{-A}) \tag{4}$$

when imported Lambert-Beer law ($A = \varepsilon \cdot C \cdot L$), the equation becomes.

$$P_a = E_e \cdot S \cdot (1 - 10^{-\varepsilon \cdot C \cdot L}) \tag{5}$$

$\boldsymbol{A}$ Corresponding absorbance of test solution at the irradiation wavelength

$\boldsymbol{E_e}$ Intensity of incident light at the irradiation wavelength

$\boldsymbol{S}$ Cross-sectional area of irradiation

$\boldsymbol{\varepsilon}$ Molar absorption coefficient

$\boldsymbol{C}$ Concentration increases of the aldehyde-hydrazone cage

$\boldsymbol{L}$ Optical path length

The energy of a photon $\boldsymbol{E_p}$ is calculated by Eq. 6.

$$E_p = \frac{h \cdot c}{\lambda} \tag{6}$$

$\boldsymbol{h}$ Planck's constant

$\boldsymbol{c}$ Speed of light

λ Irradiation wavelength

The procedure for the measurement followed steps below

5.0 mL DMSO solution of our synthesized photocage (10 μM) in a flat-bottomed quartz tube was exposed to light irradiation at 365 nm under ambient condition. The inner diameter of the flat-bottomed tubes was measured by micrometer and calculated by the formula for circular area (2.270 cm^2). The light source operated with a current stabilizer. The incident light intensity was measured with a power-meter (WATTCAS WP-TEC-1020SL, China).

A 0.5-μL portion of this solution was then subjected to UPLC-MS analysis following the photodegradation. The area of peaks from the TCI trace was integrated, and the concentrations of the product were quantified by pure aldehyde as reference (0.1, 1, 10, 100 μM).

Molar absorption coefficient measurements

Determination of the molar absorption coefficient: Initially, we calibrated the instrument using potassium dichromate standard according to European Pharmacopoeia 6.0, Chapter 2.2.25[48] [Absorption spectrophotometry, ultraviolet and visible]. To prepare stock solutions of compounds **TP2, CM2, FY4, PC1**, and **BW3**, ~1.02 mg of each sample was accurately weighed using an analytical balance and dissolved in 1 mL of DMSO in a 5-mL centrifuge tube. Serial dilutions were subsequently prepared from these stock solutions. Appropriate concentrations were selected, and the absorption spectra of the solutions were recorded over the range of 300–800 nm using the Hitachi UH5300 *UV-Vis* spectrophotometer. Baseline correction was applied prior to data analysis. The molar absorption coefficients at various wavelengths were calculated from the absorbance measurements using the Beer-Lambert law:

$$\varepsilon_{\text{exp}} = \frac{A}{c \cdot l}$$

where $\boldsymbol{\varepsilon}$ is the molar absorption coefficient ($L \cdot mol^{-1} \cdot cm^{-1}$), $\boldsymbol{A}$ is the absorbance, $\boldsymbol{c}$ is the concentration (mol/L), and $\boldsymbol{l}$ is the path length (cm).

Irradiation experiments

Irradiation experiments were done in 1.0-cm quartz fluorescence cuvette. Light source was operated by the photoreaction instrument (WP-TEC-1020SL), was purchased from WATTCAS (China).

NMR spectroscopy

NMR spectra of compounds **PC1, TP2, FY1-4, BW2**, and **BW3MP** were acquired on a JNM-ECZ600R/S1 600 MHz, and others were acquired on a Bruker AVANCE NEO 400 MHz spectrometer in DMSO-d_6 at ambient temperature with tetramethylsilane (TMS) as an internal standard. NMR standards used were as follows: (^{1}H NMR) DMSO-d_6 = 2.50 ppm. (^{13}C-NMR) DMSO-d_6 = 39.52 ppm. All chemical shifts (δ) are reported in ppm relative to TMS. Spin multiplicities were reported as a singlet (s), doublet (d), triplet (t), quartet (q), multiplet (m), and broad (br) with coupling constant (J) reported in Hz.

In vitro detection of ROS

The production of ROS under laser irradiation was detected by DCFH-DA. The 96-well plate was added with 100 μL of PBS solution containing **BW3MP** (100 μM). Then the PBS solution was exposed to dark or 660 nm laser irradiation (150 $mW \cdot cm^{-2}$) for different durations ranging from 0 to 40 min. The fluorescence intensity of DCFH-DA (ROS levels) in PBS was detected using a multifunctional microplate reader (TECAN, M200 PRO, Switzerland) with excitation at 488 nm and emission at 529 nm.

Fluorescence microscopy

Cell culture and imaging. Add 1 mL of culture medium and ~100 μL of the MCF-7 cell suspension, then incubate overnight in a cell culture incubator. The MCF-7 cell line, a human epithelial breast cancer cell line (ATCC® HTB-22™), was originally derived in 1973 by Dr. Herbert Soule at the Michigan Cancer Foundation from the pleural effusion of a 69-

year-old Caucasian female patient diagnosed with metastatic adenocarcinoma. The next day, wash the cells with PBS 1–2 times, replace the medium with 1 mL of fresh culture medium, add the test compound at a concentration of 1 μL/mL of medium, mix well, and incubate for 30 min. After incubation, wash the cells once with PBS and replace the medium with 1 mL of normal culture medium for continued incubation. Images were immediately acquired using a confocal microscope (Leica, STELLARIS 5, Germany), employing consistent acquisition parameters across all experimental groups. (Blue channel: λ_{ex}: 405 nm; λ_{em}: 430–480 nm; Green channel: λ_{ex}: 488 nm; λ_{em}: 500–530 nm; Red channel: λ_{ex}: 638 nm; λ_{em}: 650–750 nm; Scale bar: 10 μm). For the cell imaging light irradiation experiments, the instrument's built-in light source was directly applied at an intensity of 120 $mW{\cdot}cm^{-2}$.

Colocalization experiment. MCF-7 cells were cultured on a confocal dish for 24 h. Subsequently, the culture medium was replaced with a medium containing 10 μM **BW3MP** and 200 nM Lyso-Tracker Red (C1046) (Beyotime, China). After incubation for 30 min, these cells were washed with PBS and resuspended in fresh medium. Images were immediately acquired using a confocal microscope (Leica, STELLARIS 5, Germany), employing consistent acquisition parameters across all experimental groups.

CCK-8 assay

For the dark cytotoxicity. MCF-7 cells were seeded in flat-bottomed 96-well plates with the number of 7500 cells per well in the presence of 100 μL complete culture media for 24 h. The cell numbers were detected by hemocytometer count in cell suspension. After being washed with PBS three times, the MCF-7 cells were incubated with different concentrations (0, 0.1, 1, 10, 50, 100 μM) of **FY4** and **CM2**. All stock solutions were prepared in DMSO (2 mM) and diluted with complete medium. After cultured for 24 h, the cells were washed with PBS 3 times. 10 μL Cell Counting Kit-8 (CCK-8) solution and 90 μL PBS were added per well simultaneously. After another 1-h culture, the absorbance at 450 nm was read by 96-well plate reader.

For the phototoxicity comparison between hydrazone-based photocages. MCF-7 cells were seeded in flat-bottomed 96-well plates with the number of 7500 cells per well in the presence of 100 μL complete culture media for 24 h. After washed with PBS three times, the MCF-7 cells were incubated with different concentrations (0, 0.1, 1, 10, 50, 100 μM) of **FY4** and **CM2**, and (0, 0.01, 0.05, 0.1, 0.5, 1, 5, 10 μM) of BW3STS. All stock solutions were prepared in DMSO (2 mM) and diluted with complete medium. After cultured for 24 h, the cells were washed with PBS three times. Then the cells were get irradiated for 20 min. After cultured for 24 h, 10 μL Cell Counting Kit-8 (CCK-8) solution and 90 μL PBS were added per well simultaneously. After another 1-h culture, the absorbance at 450 nm was read by 96-well plate reader.

Data availability

The data supporting the findings of this study are available in the article and Supplementary Information or from the lead contact upon reasonable request. Cartesian coordinates (x, y, z) for all the compounds are provided in Suppelmentary Data 1. All figure data in the main text can be found in Supplementary Data 2, while the data in the Supplementary Information are provided in Supplementary Data 3. NMR and high-resolution mass spectrometry data are also included in Supplementary Data 4. Further information and requests for resources and reagents should be directed to and will be fulfilled by the lead contact, L.X. (Lijunxie8224@outlook.com).

Code availability

The codes supporting the computational studies of this study are available in the Supplementary Information or from the lead contact upon reasonable request.

Received: 22 December 2024; Accepted: 15 May 2025;
Published online: 07 June 2025

References

1. Li, Y. et al. Recent progress in studies of photocages. *Smart Mol.* **1**, e20220003 (2023).
2. Liu, T. et al. Photo-responsive polymers based on o-nitrobenzyl derivatives: from structural design to applications. *Prog. Polym. Sci.* **146**, https://doi.org/10.1016/j.progpolymsci.2023.101741 (2023).
3. Mukhtar, A. et al. Excited state complexes of coumarin derivatives. *J. Fluoresc.* **32**, https://doi.org/10.1007/s10895-021-02807-z (2022).
4. Gomez, A. M. & Cristobal Lopez, J. Bringing color to sugars: the chemical assembly of carbohydrates to BODIPY dyes. *Chem. Rec.* **21**, 3112 (2021).
5. Sadeghpour, M. et al. Recent progress on the synthesis of henna-based dibenzoxanthenes. *New J. Chem.* **45**, 13669 (2021).
6. Jiang, L. et al. Sanger's reagent as a new general phototrigger for organelle imaging. *Sens. Actuator B Chem.* **398**, 134742 (2024).
7. Wong, P. et al. Photocontrolled release of doxorubicin conjugated through a thioacetal photocage in folate-targeted nanodelivery systems. *Bioconjugate Chem.* **28**, 3016 (2017).
8. Paul, A. et al. Mitochondria-localized in situ generation of rhodamine photocage with fluorescence turn-on enabling cancer cell-specific drug delivery triggered by green light. *Chem. Commun.* **56**, 8412 (2020).
9. Shin, J. et al. Mitochondria-targeted nanotheranostic: harnessing single-laser-activated dual phototherapeutic processing for hypoxic tumor treatment. *Matter* **4**, 2508 (2021).
10. Shao, Q. et al. Design of a prodrug photocage for cancer cells detection and anticancer drug release. *Talanta* **274**, https://doi.org/10.1016/j.talanta.2024.126002 (2024).
11. Ma, J. et al. Intracellular delivery and deep tissue penetration of nucleoside triphosphates using photocleavable covalently bound dendritic polycations. *Chem. Sci.* **15**, 6478 (2024).
12. Yao, W. et al. O-nitrobenzyl liposomes with dual-responsive release capabilities for drug delivery. *J. Mol. Liq.* **334**, 116016 (2021).
13. Peterson, J. A. et al. A family of BODIPY photocages cleaved by single photons of visible/near-IR light. *J. Am. Chem. Soc.* **140**, 7343 (2018).
14. Qin, Y. et al. Construction of covalent organic cages with aggregation-induced emission characteristics from metallacages for mimicking light-harvesting antenna. *Angew. Chem. Int. Ed*. **62**, https://doi.org/10.1002/anie.202308210 (2023).
15. Wang, L. S. et al. Oxime as a general photocage for the design of visible light photo-activatable fluorophores. *Chem. Sci.* **12**, 15572 (2021).
16. Xiong, H. et al. Photo-controllable biochemistry: exploiting the photocages in phototherapeutic window. *Chem*. **9**, 29 (2023).
17. Chaudhuri, A. et al. Bimane: a visible light induced fluorescent photoremovable protecting group for the single and dual release of carboxylic and amino acids. *Org. Lett.* **19**, 1598 (2017).
18. Sebej, P. et al. Fluorescein analogues as photoremovable protecting groups absorbing at ~520 nm. *J. Org. Chem.* **78**, 1833 (2013).
19. Situ, Z. et al. Boosting the release of leaving group from blebbistatin derivative photocages via enhancing intramolecular charge transfer and stabilizing cationic intermediate. *J. Phys. Chem. Lett.* **14**, 11580 (2023).
20. Ray et al. Visible light-responsive delivery of two anticancer drugs using single-component fluorescent organic nanoparticles. *ACS Appl. Nano Mater.* **5**, 7512 (2022).
21. Wei, T. et al. Sanger's reagent sensitized photocleavage of amide bond for constructing photocages and regulation of biological functions. *J. Am. Chem. Soc.* **142**, 3806 (2020).
22. Zhou, C. et al. Photoactivatable nanobody conjugate dimerizer temporally resolves Tiam1-Rac1 signaling axis. *Adv. Sci*. **11**, https://doi.org/10.1002/advs.202307549 (2024).

23. Vorobev, A. Y. & Moskalensky, A. E. Long-wavelength photoremovable protecting groups: on the way to in vivo application. *Comput. Struct. Biotechnol. J.* **18**, 27 (2020).
24. Su, X. & Aprahamian, I. Hydrazone-based switches, metallo-assemblies and sensors. *Chem. Soc. Rev.* **43**, 1963 (2014).
25. Yang, J. et al. Synthesis, optical properties, determination and imaging in living cells and bamboo of cinnamaldehyde derivatives. *Spectrochim. Acta A* **255**, 119730 (2021).
26. Zhang, T., Huang, Y. & Chen, X. Tetraphenylethylene-based AIE nanoprobes for labeling lysosome by two-photon imaging in living cells. *Spectrochim. Acta A* **306**, 123630 (2024).
27. Feng, X. et al. Aggregation behaviour of pyrene-based luminescent materials, from molecular design and optical properties to application. *Chem. Soc. Rev.* **52**, 6715 (2023).
28. Krupka, O. & Hudhomme, P. Recent advances in applications of fluorescent perylenediimide and perylenemonoimide dyes in bioimaging, photothermal and photodynamic therapy. *Int. J. Mol. Sci.* **24**, 6308 (2023).
29. Omura, S. et al. Staurosporine, a potentially important gift from a microorganism. *ChemInform* **26**, 535–548 (1995).
30. Omura, S. et al. Staurosporine: new lease of life for parent compound of today's novel and highly successful anti-cancer drugs. *J. Antibiot.* **71**, 688 (2018).
31. Park, B. S. et al. Staurosporine analogues from microbial and synthetic sources and their biological activities. *Curr. Med. Chem.* **20**, 3872 (2013).
32. Jeet, K. & Ronald, T. et al. Hydrolytic stability of hydrazones and oximes. *Angew. Chem. Int. Ed.* **47**, 7523 (2008).
33. Katoh, R., Kubota, H. & Sugawara, K. Absorption spectra of 1-methylnaphthalene, anthracene, pyrene, and perylene in the liquid phase. *Chem. Phys. Lett*. **844**, https://doi.org/10.1016/j.cplett.2024.141263 (2024).
34. Alabugin, I. V., Gabriel, D. P. G. & Abdo, M. A. Hyperconjugation. *Wires Comput. Mol. Sci.* **9**, 1389 (2019).
35. Wang, C. et al. Twisted intramolecular charge transfer (TICT) and twists beyond TICT: from mechanisms to rational designs of bright and sensitive fluorophores. *Chem. Soc. Rev.* **50**, 12656 (2021).
36. Bala, I. et al. Multi-stage and multi-colour liquid crystal reflections using a chiral triptycene photoswitchable dopant. *Nat. Chem.* **16**, 2084–2090 (2024).
37. Niu, H. et al. Photoinduced electron transfer (PeT) based fluorescent probes for cellular imaging and disease therapy. *Chem. Soc. Rev.* **52**, 2322 (2023).
38. Zhang, Z. et al. Isomerization of bioactive acylhydrazones triggered by light or thiols. *Nat. Chem.* **15**, 1285 (2023).
39. Baah, S. et al. Antibody-drug conjugates—a tutorial review. *Molecules* **26**, 2943 (2021).
40. Nikolova-Mladenova, B. et al. Design, synthesis and cytotoxic activity of novel salicylaldehyde hydrazones against leukemia and breast cancer. *Int. J. Mol. Sci*. **24**, https://doi.org/10.3390/ijms24087352 (2023).
41. Zhao, J. et al. A salicylaldehyde benzoyl hydrazone based near-infrared probe for copper(II) and its bioimaging applications. *RSC Adv.* **12**, 3073 (2022).
42. Mukherjee, S. & Betal, S. Sensing phenomena, extraction and recovery of Cu^{2+} followed by smart phone application using a luminescent pyrene based chemosensor. *J. Lumin.* **204**, 145 (2018).
43. Wang, C. et al. Quantitative design of bright fluorophores and AIEgens by the accurate prediction of twisted intramolecular charge transfer (TICT). *Angew. Chem. Int. Ed*. **59**, https://doi.org/10.1002/anie.201916357 (2020).
44. Li, Y. et al. Development and challenge of fluorescent probes for bioimaging applications: from visualization to diagnosis. *Top. Curr. Chem*. **380**, https://doi.org/10.1007/s41061-022-00376-8 (2022).
45. Ram, K. & Anastasio, C. Photochemistry of phenanthrene, pyrene, and fluoranthene in ice and snow. *Atmos. Environ.* **43**, 2252 (2009).
46. Tsuchikama, K. et al. Exploring the next generation of antibody-drug conjugates. *Nat. Rev. Clin. Oncol.* **21**, 203 (2024).
47. Hamann, P. R. et al. Gemtuzumab ozogamicin, a potent and selective anti-CD33 antibody-calicheamicin conjugate for treatment of acute myeloid leukemia. *Bioconjugate Chem*. **13**, https://doi.org/10.1021/bc010021y (2002).
48. European Pharmacopoeia 6.0. 2.2.25. Absorption spectrophotometry, ultraviolet and visible. (EDQM, 2008).

Acknowledgements

This work was supported by Department of Science and Technology of Fujian Province (Grant Number 2024R1043); the National Natural Science Foundation of China (NSFC, Grant Numbers 81703555 and 81961138017).

Author contributions

Xia Wang: investigation, writing—original draft, software, formal analysis, analysis data, writing—review & editing. Jingming Zhou: writing—original draft, analysis data, writing—review & editing. Yu Cheng: investigation, funding acquisition. Hongmei Wu: investigation. Xuejing Su: investigation. Rundong Wang: investigation. Kaiyan Xiao: investigation. Weiwei Zhang: writing—review & editing. Zhong Chen: funding acquisition, supervision. Bing Xu: writing—review & editing. Yusheng Lu: analysis of data and funding acquisition. Hongqiang Qiu: supervision, funding acquisition. Lijun Xie: conceptualization, methodology, funding acquisition, supervision.

Competing interests

The authors declare no competing interests.

Additional information

Supplementary information The online version contains supplementary material available at https://doi.org/10.1038/s42004-025-01561-8.

Correspondence and requests for materials should be addressed to Yusheng Lu, Hongqiang Qiu or Lijun Xie.